Supplementary Information (SI) for Journal of Materials Chemistry A.
This journal is © The Royal Society of Chemistry 2024

Supporting Information for

Improving the Electrocatalytic Activity of Cobalt Oxide with Bismuth for Acidic Oxygen Evolution Reaction

Experimental Procedure

Chemicals

All chemicals used for the work were of reagent-grade and purchased from Sigma-Aldrich. They included bismuth(III) nitrate pentahydrate ($Bi(NO_3)_3{\cdot}5H_2O$) (>98%), cobalt(II) nitrate hexahydrate ($Co(NO_3)_2{\cdot}6H_2O$) (>98%), nickel(II) nitrate hexahydrate ($Ni(NO_3)_2{\cdot}6H_2O$) (>99%), iron(III) nitrate nonahydrate ($Fe(NO_3)_3{\cdot}9H_2O$) (>99%), citric acid (99%, Sigma Aldrich), perchloric acid ($HClO_4$), (70%), and nitric acid (HNO_3) (70%).

Working Electrode Substrates

Fluorine-doped tin(IV) oxide (FTO)-coated glass slides (with a dimension of length × width × thickness = 300 mm × 300 mm × 2.2 mm and surface resistivity of ~7 Ω/sq) were obtained from Sigma-Aldrich, and they were used as substrates to produce the electrocatalysts or working electrodes studied. Beforehand, the FTO slides were cut into 1.2 cm × 1.2 cm (length × width) and cleaned by soaking them in ethanol for 30 min, and then drying them in air at room temperature for 5 min. Each working electrode was set to have an effective, measurable electroactive area of 1.2 cm × 0.7 cm.

Synthesis of Bismuth-doped Cobalt Oxides on FTO Glass Slides

A series of bismuth-doped cobalt oxides (Bi-doped cobalt-oxides) were synthesized directly on FTO by thermal decomposition of solutions of metal nitrates in citric acid and a small amount of nitric acid. Briefly, metal nitrates with a total amount of 0.45 mmol but with different ratios of Co:Bi (namely, 1:0,14:1, 9:1, 2:1, 1:2, and 0:1), nitric acid (6 M, 50 µL) and citric acid solution (0.75 M, 950 µL) were mixed. Then, 50 µL of the solution was dropped onto the effective electroactive area of FTO and dried at 100 °C for 10 min. The FTO-coated materials were then annealed at 400 °C for 12 h, and after which the less firmly attached parts of the materials were removed by gently tapping the FTO on a hard surface. The resulting, black-colored thin films containing the deposited catalysts on the FTO substrates were named as $Co_aBi_bO_x$, where a:b represent the mole ratios of the Co and Bi, respectively, in their corresponding precursors.

By following the same procedure, Bi-doped iron oxides and Bi-doped nickel oxides with the same ratios of Bi and the respective metals, as discussed in more detail in the

paper, were synthesized on the FTO substrates.

Characterizations

X-ray diffraction (XRD) pattern of the catalysts on FTO were recorded with a Bruker D2 Phaser 2nd Generation Benchtop Diffractometer that has an air-cooled sealed X-ray tube equipped with Cu anode (1.54 Å wavelength) and an X-ray source that is operating at 300 Watts (30 keV and 10 mA). Each XRD pattern is obtained with a step size of 0.02° and a scan rate of 0.02°/s. To determine the morphologies and elemental compositions of the metals in the catalysts, field emission scanning electron microscope (FESEM) images and energy-dispersive X-ray spectroscopy (EDS) elemental mapping images were acquired with a Zeiss Sigma field emission scanning electron microscope that is equipped with an EDS detector (Oxford). The X-ray photoelectron spectroscopy (XPS) studies were performed on the catalysts on FTO substrates with a K-Alpha™ XPS spectrometer (Thermo Fisher Scientific™) that was operated with Al Kα X-ray source (hv =1486.6 eV). The XPS survey spectra were obtained by scanning them with an energy resolution of 1 eV while the high-resolution spectra were obtained by scanning them with an energy resolution of 0.1 eV. All the binding energy in XPS spectra were calibrated with C 1s peak (at a binding energy = 284.8 eV) associated with the adventitious carbon present on the materials.

Electrochemical Measurements and Electrocatalytic Tests

All electrochemical measurements were performed using VersaSTAT 3 Potentiostat-Galvanostat (Princeton Applied Research) that has a VersaStudio software. To perform the measurement, a three-electrodes system was used, and the potential was measured using a saturated calomel electrode (SCE) ($Hg|Hg_2Cl_2|KCl_{(sat)}$, 0.242 V vs RHE) as a reference electrode and a graphite rod as a counter electrode. The FTO-deposited catalysts were used as the working electrodes, and $HClO_4$ solution (0.1 M, pH = 1) was used as the electrolyte. All electrochemical measurements were performed at room temperature and under an ambient environment. The measured potentials obtained with respect to SCE were then converted to “versus reversible hydrogen electrode (RHE)” using the Nernst equation (equation 1).

$$E_{vs\,(RHE)} = E_{vs(SCE)} + 0.242 + 0.059 \times pH \quad (1)$$

Multiple cyclic voltammetry (CV) scans were first carried out for each catalyst to activate and stabilize it before recording its CV curve. In the case of Bi-doped cobalt oxide, five CV scans were carried out in the potential range of 1.3 V to 2.1 V (vs RHE) at scan rate of 50 mV/s. The linear sweep voltammetry (LSV) curve in each case was then obtained at a scan rate of 5 $mV.s^{-1}$ and in the same potential range. The overpotentials at a current density of 10 $mA{\cdot}cm^{-2}$ and the Tafel slope, which usually has a negative correlation with the kinetics for electrocatalytic reaction, were then calculated based on the LSV curve. The latter was obtained using the Tafel equation ($\eta = b \times \log j + a$), where η is the overpotential, j is the current density, and b is the Tafel slope.

Electrochemical impedance spectra (EIS) were recorded by sweeping the frequency from 50 kHz to 0.1 Hz at an applied potential of 1.60 V vs. RHE and using an AC perturbation of 20 mV. Nyquist plots were obtained directly using the software present in the EIS spectrometer. The diameters of the plots have an inverse correlation with the electron mobility.

The electrochemical capacitance of each catalyst was obtained by scanning the potential from 0.747 V to 0.846 V (vs. RHE) in the non-faradaic region at seven different scan rates, namely, 20, 40, 60, 80, 100, 120, and 140 $mV.s^{-1}$. The electrochemical capacitance of each catalyst (C_{dl}) was then determined from the slope of the respective plot of charging current density versus scan rate. The charging current density was obtained using the equation $J = J_a - J_c$, where Ja and Jc are the anodic and cathodic current densities, respectively, at 0.797 V (vs. RHE).

Theoretical Methods

The spin-polarized density functional theory (DFT) calculations were performed using MedeA VASP (Vienna Ab-initio Simulation Package) program.[1-3] Generalized gradient approximation (GGA) with the Perdew-Burke-Ernzerhof (PBE) functional was employed for describing the exchange correlation interactions.[4] Van der Waals interactions were considered by using the DFT-D3 approach.[5] The calculations utilized a plane-wave cutoff energy set to 400 eV. For geometry optimization, the convergence criteria for energy and force are 1×10^{-5} eV and 0.02 eV/A, respectively. The k-point mesh was set as 5 x 5 x 5 for bulk calculation and 2 x 4 x 1 for Co_3O_4 (100) surface slabs calculation. A 15 Å vacuum layer was added onto the surface of Co_3O_4 (100) to avoid interference between slabs. During the structure optimization, the bottom two atomic layers remained fixed, while the rest of layers were allowed to relax. The DFT + U method was used for the calculation, and the value of U value was set as 3.5 for Co.[6]

The oxygen evolution reaction proceeds through the following four ($H^+ + e^-$) transfer steps:

$$H_2O + * = *OH + (H^+ + e^-)$$

$$*OH = *O + (H^+ + e^-)$$

$$*O + H_2O = *OOH + (H^+ + e^-)$$

$$*OOH = * + O_2 + (H^+ + e^-)$$

In these equations, * represents the catalyst slab. The Gibbs free energy of $G(H^+ + e^-)$ is equivalent to $1/2G(*H_2)$ according to computational hydrogen electrode (CHE) model.[7] The Gibbs free energy values of adsorbed intermediates were corrected by using VASPKIT program.[8]

Additional Results and Discussions

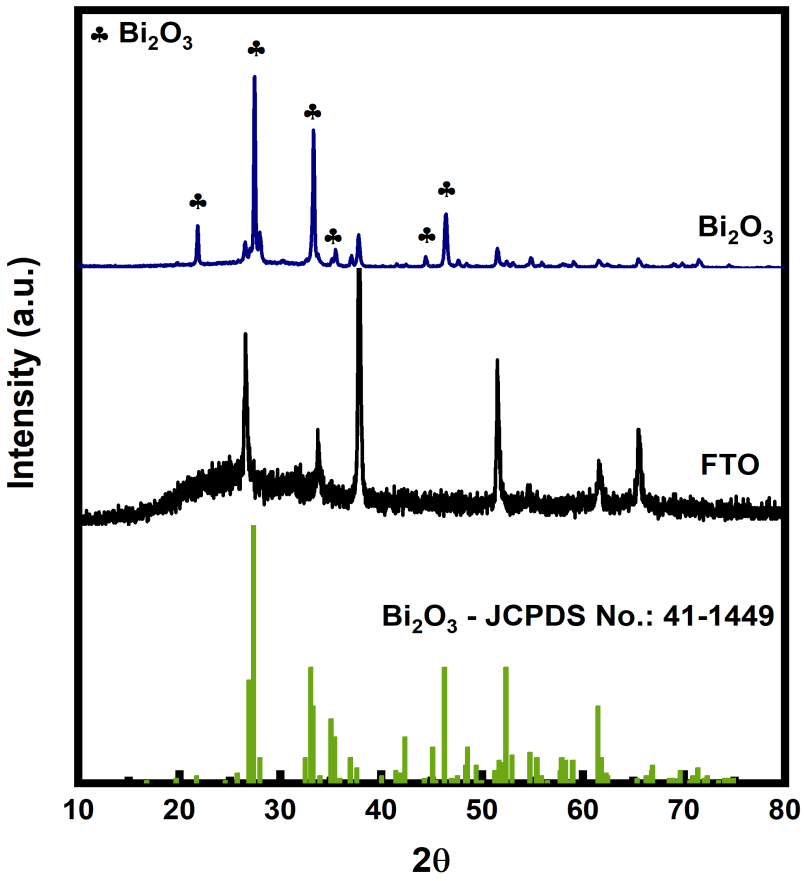

Figure S1. XRD patterns of FTO substrate and Bi_2O_3 synthesized in situ on FTO substrate. The JCPDS of Bi_2O_3 is included for reference.

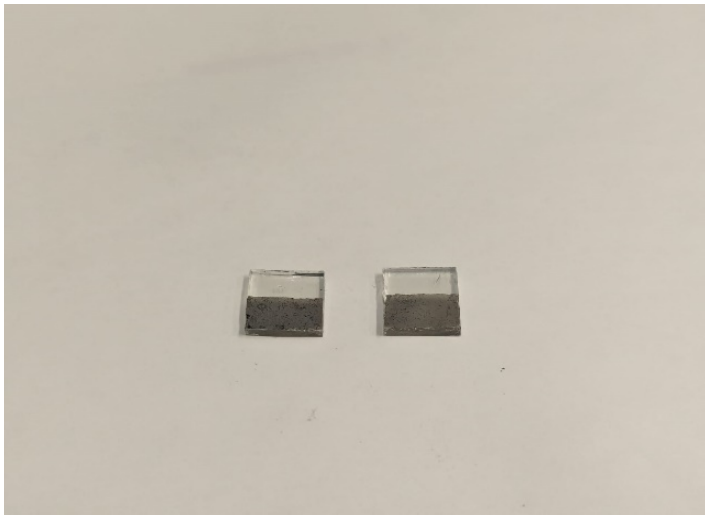

Figure S2. Digital image of the catalyst Co_9BiO_x synthesized in situ on FTO.

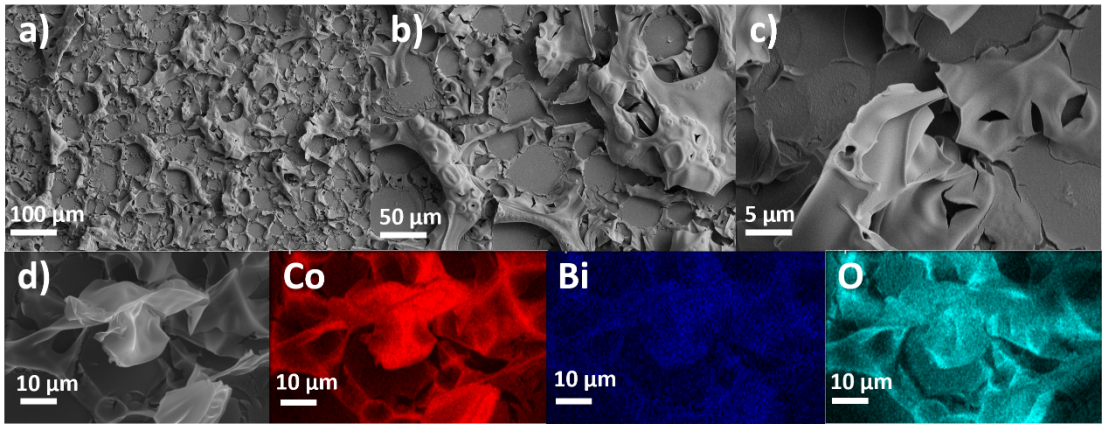

Figure S3. (a-c) FESEM images and (d) EDS elemental mapping images of $Co_{14}BiO_x$ on FTO. The EDS mapping images show that Co, Bi, and O are uniformly distributed on the catalyst.

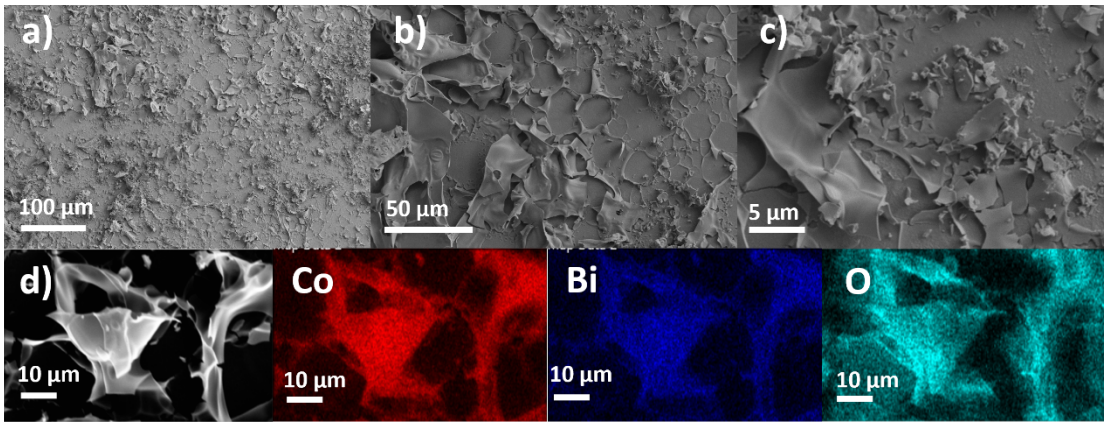

Figure S4. (a-c) FESEM images and (d) EDS elemental mapping images of Co_2BiO_x on FTO. The EDS mapping images show that Co, Bi, and O are uniformly distributed on the catalyst.

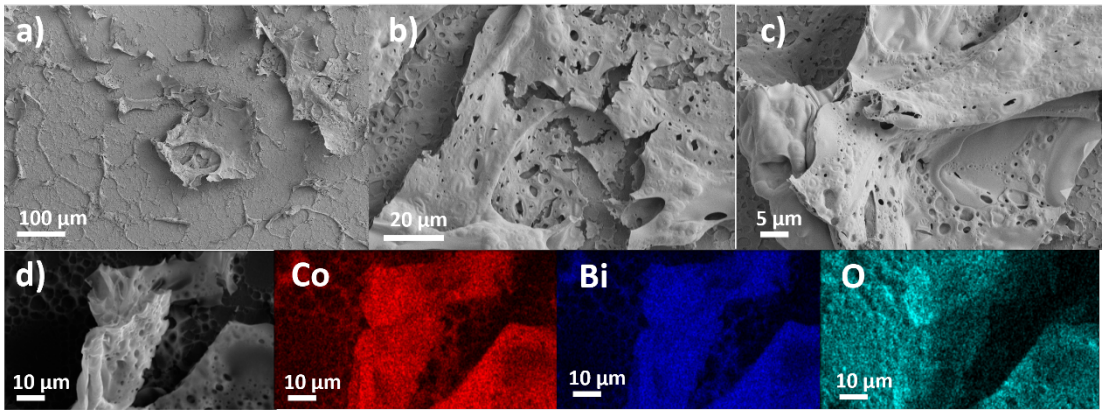

Figure S5. (a-c) FESEM images and (d) EDS elemental mapping images of $CoBi_2O_x$ on FTO. The EDS mapping images show that Co, Bi, and O are uniformly distributed on the catalyst.

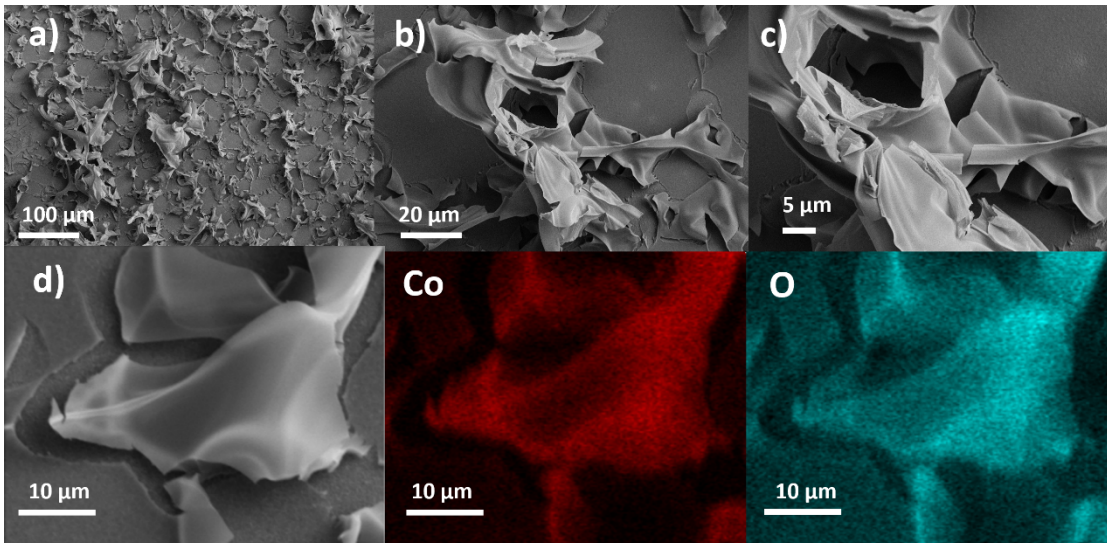

Figure S6. (a-c) FESEM images and (d) EDS elemental mapping images of Co_3O_4 on FTO. The latter show that Co, and O are uniformly distributed on the catalyst.

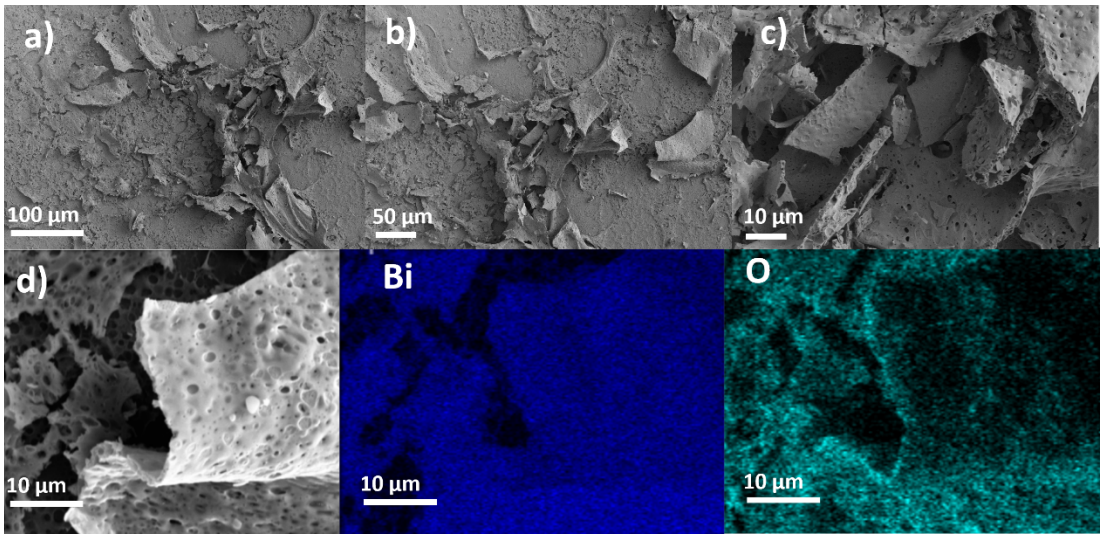

Figure S7. (a-c) FESEM images and (d) EDS elemental mapping images of Bi_2O_3 on FTO. The latter show that Bi and O are uniformly distributed on the catalyst.

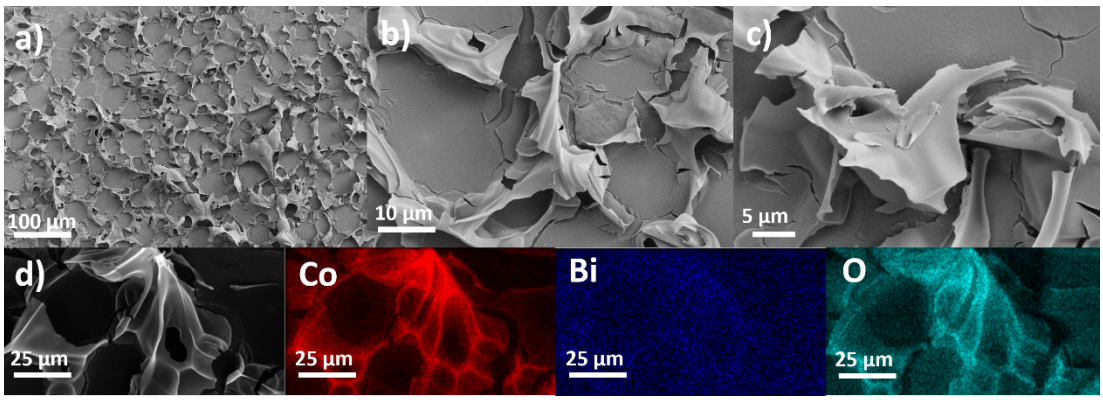

Figure S8. (a-c) FESEM images and (d) EDS elemental mapping images of Co_9BiO_x on FTO after 5 h-long chronopotentiometric test. The EDS mapping images show that Co, Bi, and O are uniformly distributed on the catalyst.

Table 1. Ratio of Co:Bi determined with EDS analysis for different catalysts present on the FTO substrates.

Catalysts	**Co:Bi**
Co_3O_4	1:0
$Co_{14}BiO_x$	12.6:1
Co_9BiO_x	8.3:1
Co_2BiO_x	2.1:1
$CoBi_2O_x$	1:2
Bi_2O_3	0:1
Co_9BiO_x after 5 h-long chronopotentiometric test	22.5:1

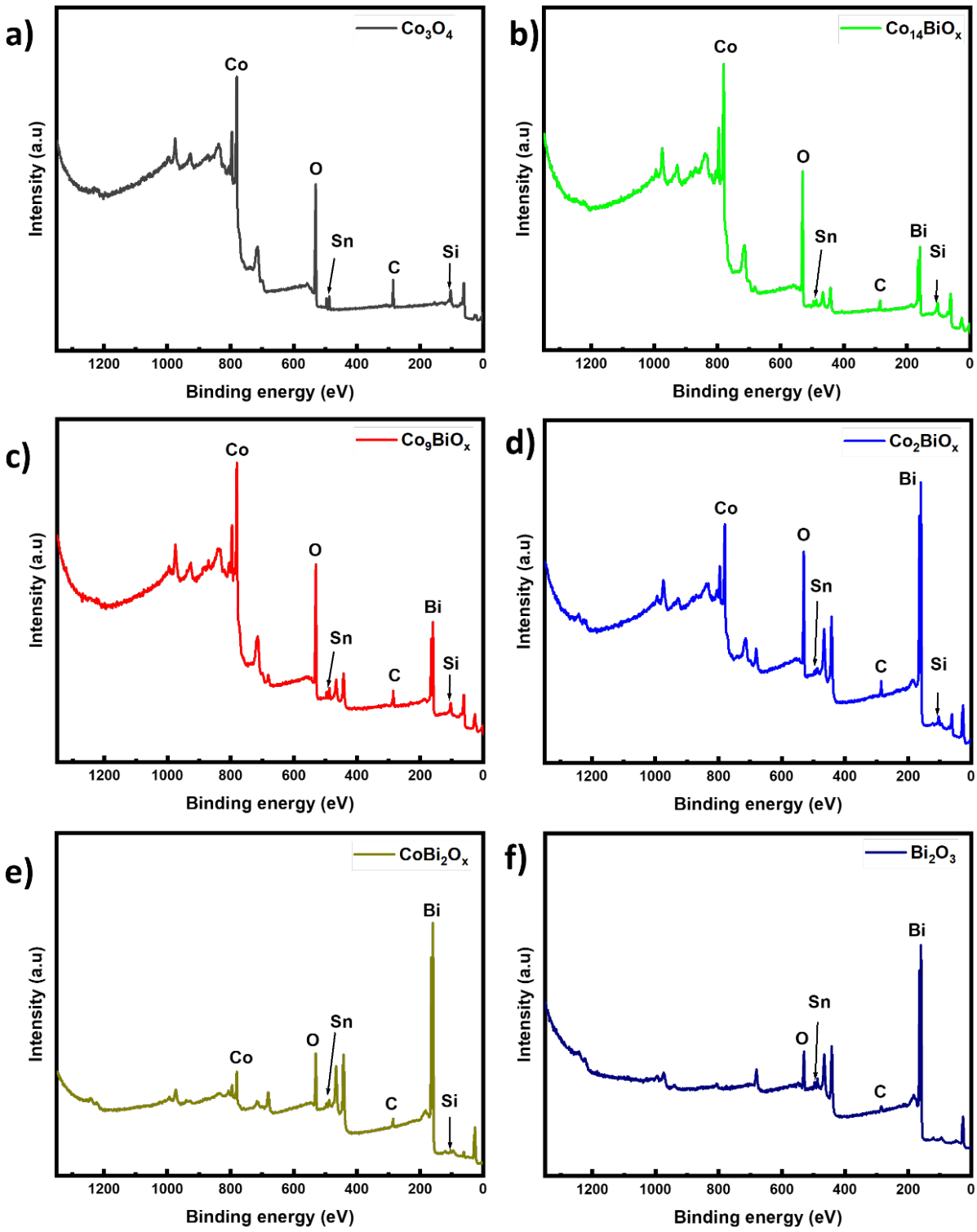

Figure S9. XPS survey spectra of the catalysts (a) Co_3O_4, (b) $Co_{14}BiO_x$, (c) Co_9BiO_x, (d) Co_2BiO_x, (e) $CoBi_2O_x$, and (f) Bi_2O_3.

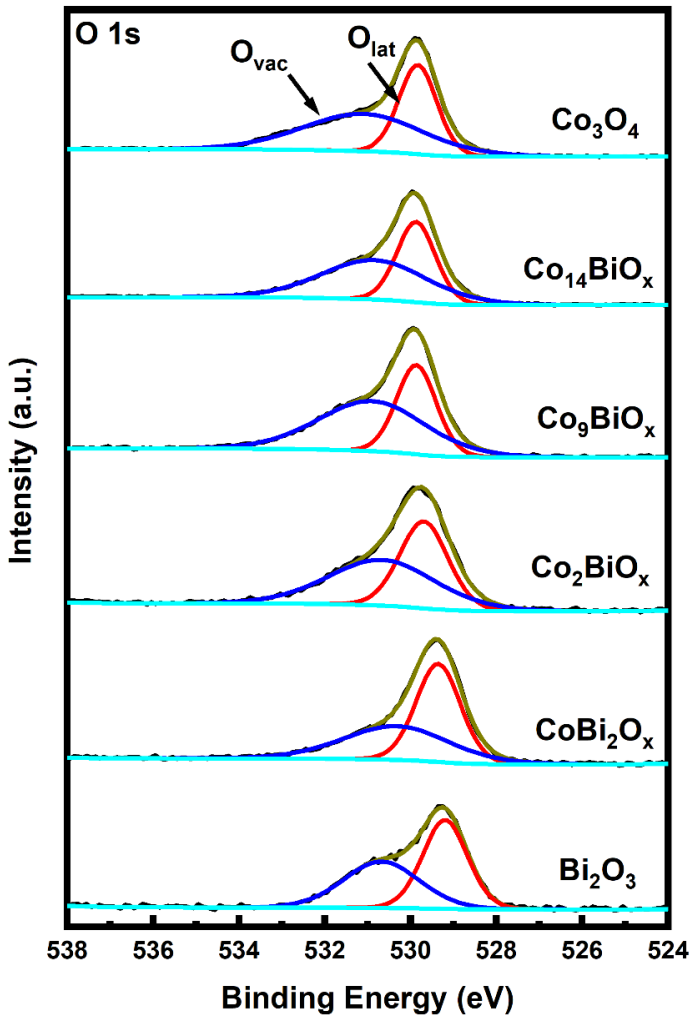

Figure S10. High resolution O 1s XPS spectra of the catalysts Co_3O_4, $Co_{14}BiO_x$, Co_9BiO_x, Co_2BiO_x, $CoBi_2O_x$, and Bi_2O_3.

Table S2. Ratios of Co:Bi determined by XPS analysis for the catalysts present on the FTO substrates are given here. Additionally, the relative ratios of the two Co oxidation states (i.e., Co^{2+} and Co^{3+}) and the relative ratio of the two Bi oxidation states (i.e., Bi^{3+} and Bi^{5+}) on the surfaces of the catalysts are determined based on the XPS analysis of Co 2p peaks and Bi 4f peaks, respectively.

Catalysts	**Co:Bi Ratio**	**Co^{2+}:Co^{3+} Ratio**	**Bi^{3+}:Bi^{5+} Ratio**
Co_3O_4	1:0	3.67	-
$Co_{14}BiO_x$	12:1	3.88	1.7
Co_9BiO_x	7.2:1	3.14	2.39
Co_2BiO_x	2:1	1.91	2.91
$CoBi_2O_x$	1:1.7	0.76	3.68
Bi_2O_3	0:1	-	-
Co_9BiO_x after 5 hour-long chronopotentiometric test	14.8:1	3.44	3.42

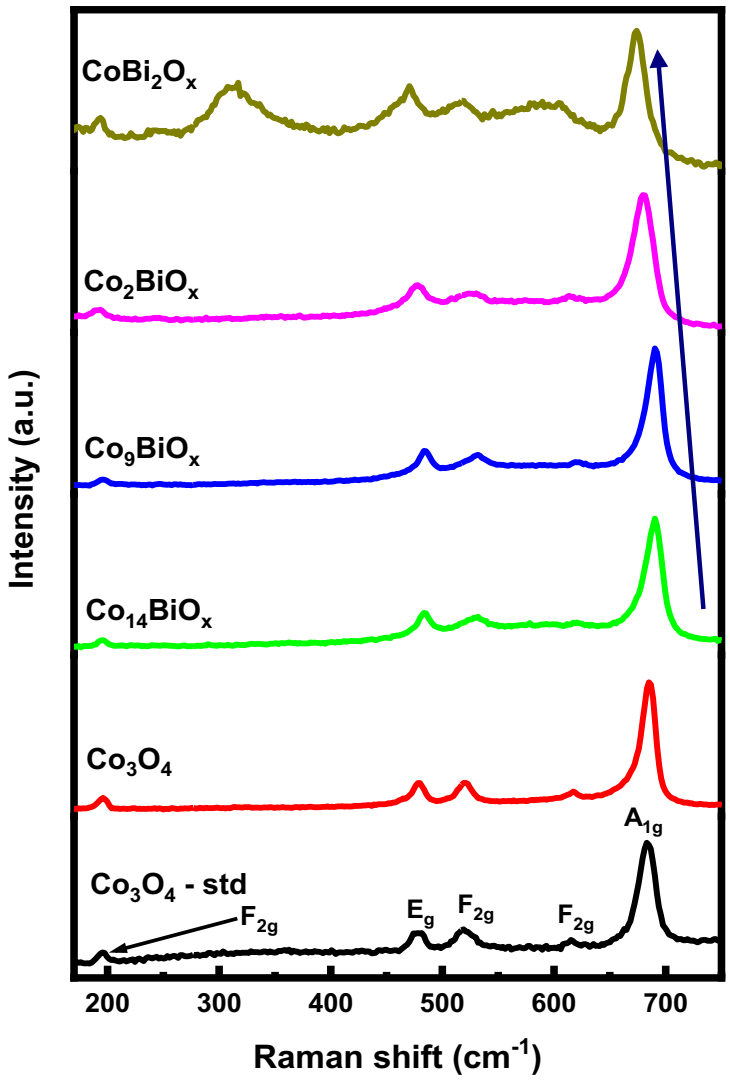

Figure S11. Raman spectra of the catalysts Co_3O_4, $Co_{14}BiO_x$, Co_9BiO_x, Co_2BiO_x, $CoBi_2O_x$ synthesized on FTO and a commercially available Co_3O_4.

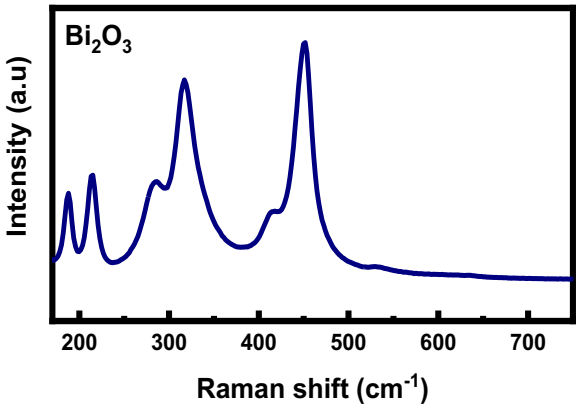

Figure S12. Raman spectrum of Bi_2O_3 on FTO.

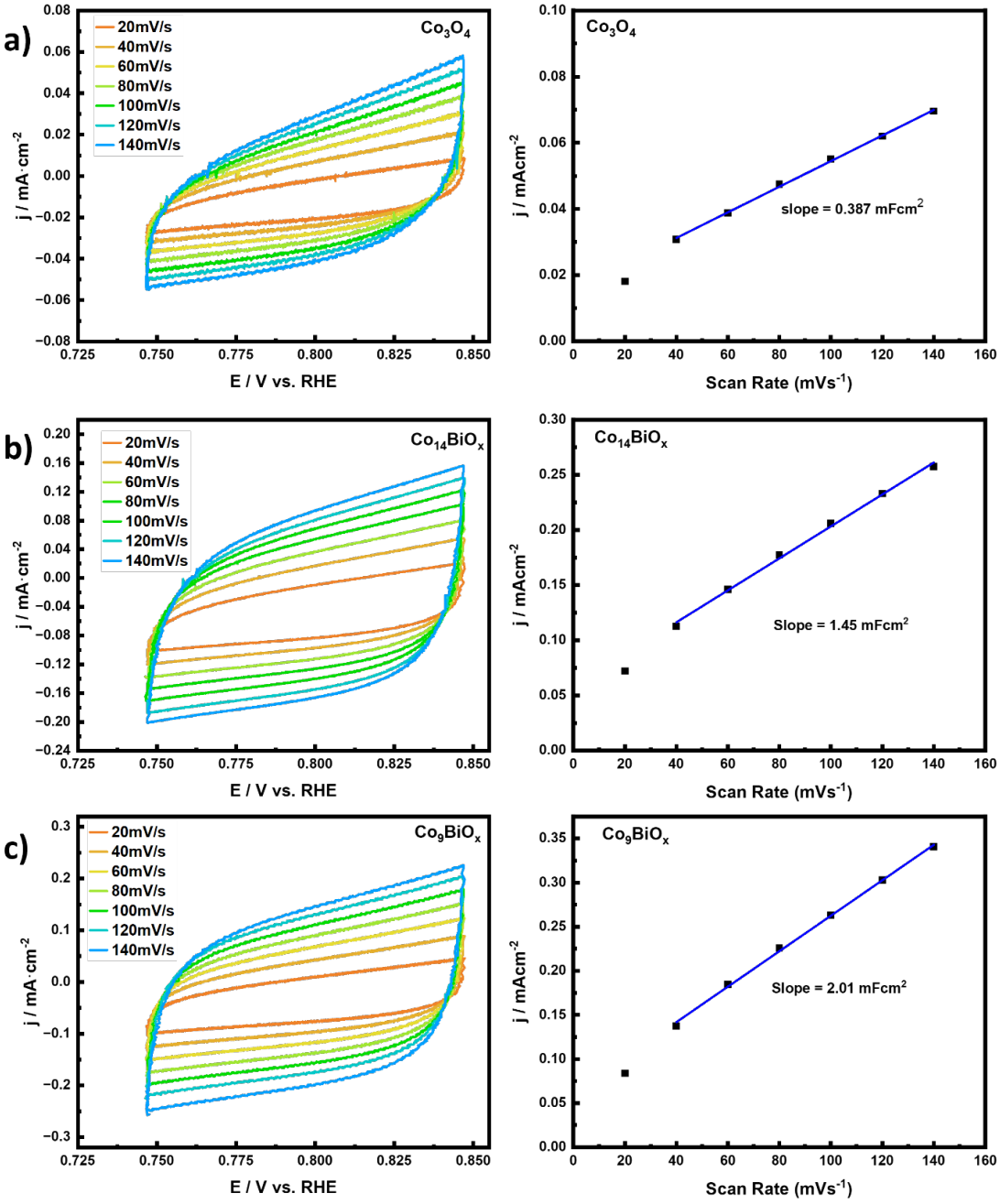
a)
20mV/s
40mV/s
60mV/s
80mV/s
100mV/s
120mV/s
140mV/s
Co3O4
j / mA·cm-2
E / V vs. RHE
Co3O4
j / mAcm-2
slope = 0.387 mFcm2
Scan Rate (mVs-1)
b)
Co14BiOx
Slope = 1.45 mFcm2
c)
Co9BiOx
Slope = 2.01 mFcm2

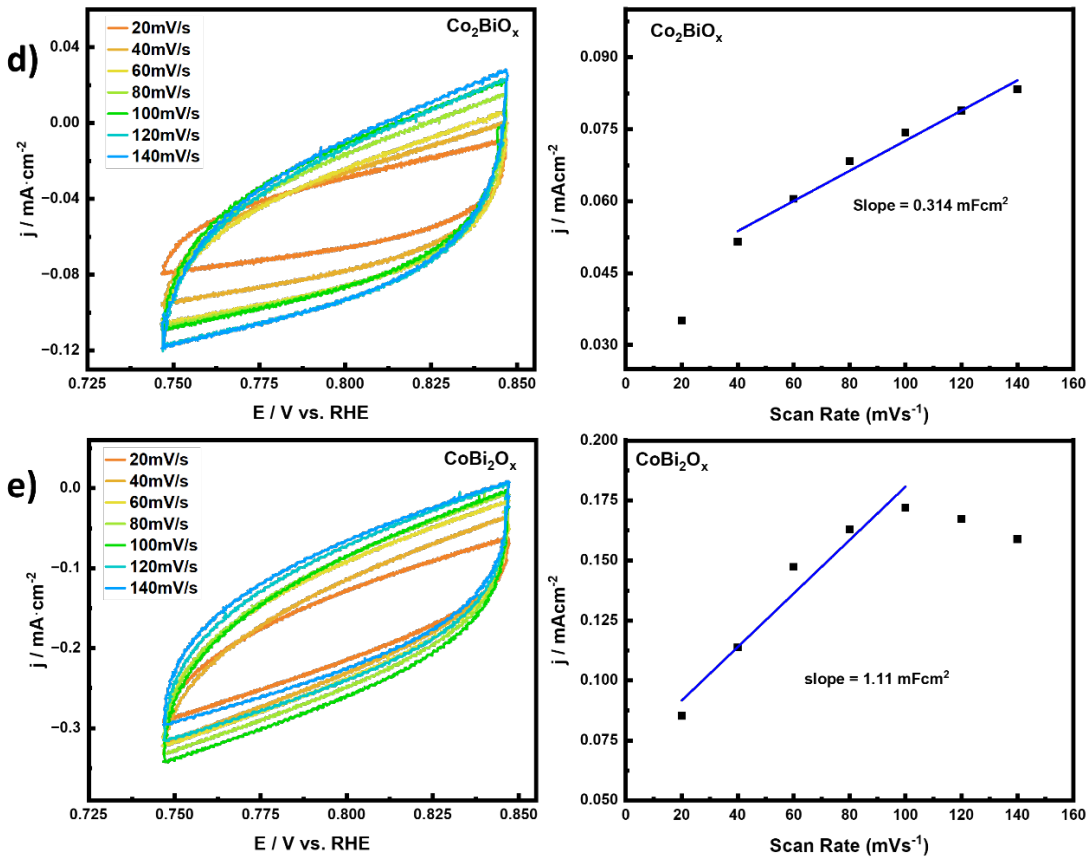

Figure S13. (Left panels) Cyclic voltammetry (CV) curves of the catalysts obtained in the non-Faradic region at scan rates of 20, 40, 60, 80, 100, 120, and 140 mV.s^{-1}, and (Right panels) the corresponding linear fit of charging current densities measured at 0.797 V vs RHE vs scan rate for (a) Co_3O_4, (b) $Co_{14}BiO_x$, (c) Co_9BiO_x, (d) Co_2BiO_x, and (e) $CoBi_2O_x$.

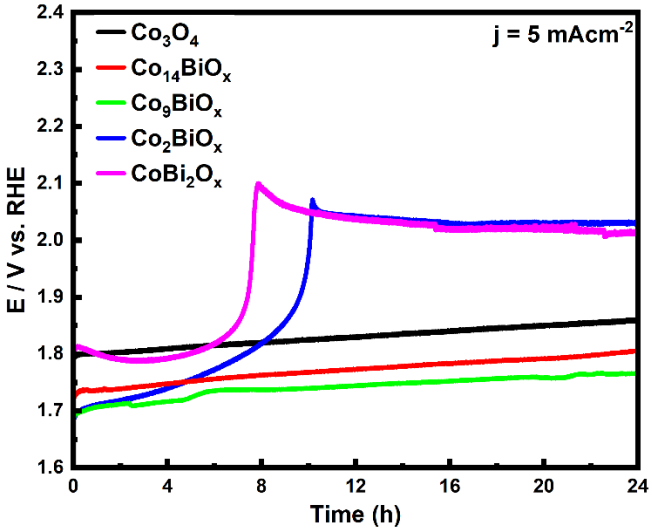

Figure S14. Chronopotentiometric profiles (or potential versus reaction time) obtained for Co_3O_4, $Co_{14}BiO_x$, Co_9BiO_x, Co_2BiO_x, and $CoBi_2O_x$ to determine their stability during electrocatalytic OER at a current density (j) of 5 mA cm^{-2}.

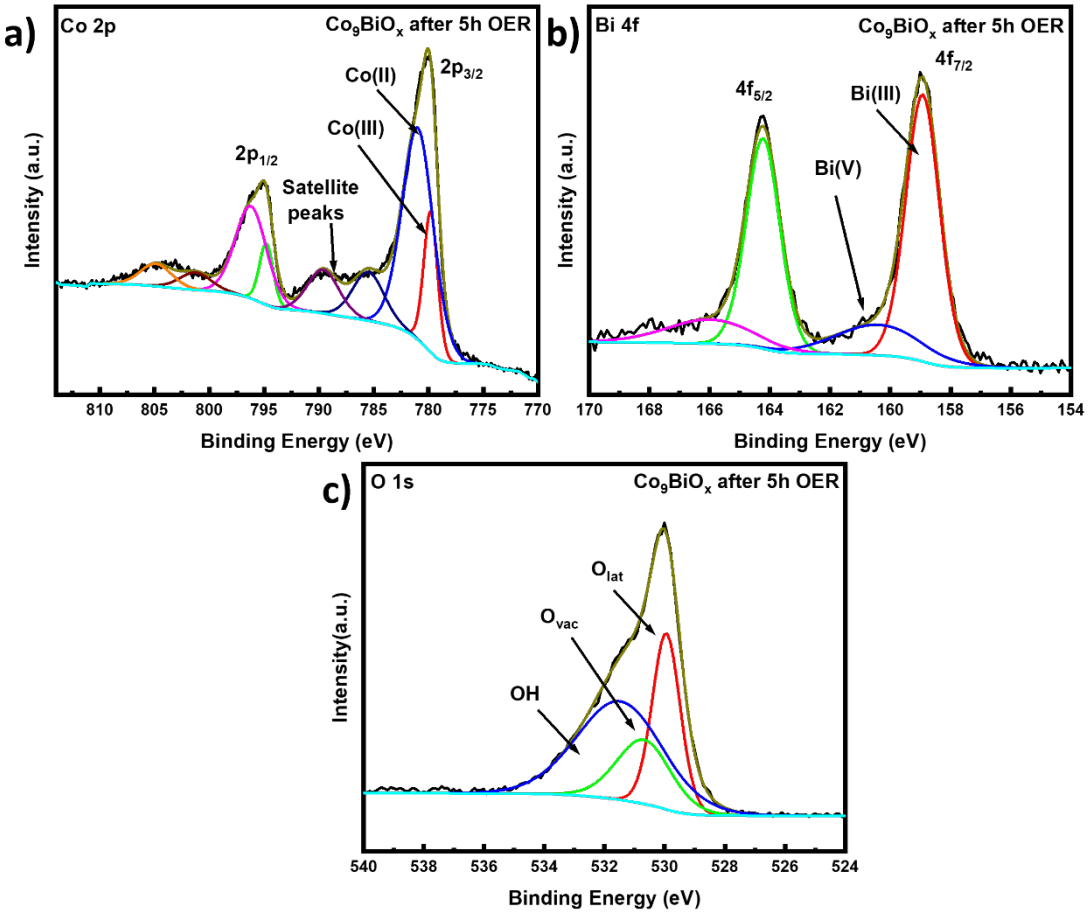

Figure S15. High resolution XPS spectra of Co_9BiO_x after 5 hour-long chronopotentiometric test showing peaks associated with (a) Co 2p, (b) Bi 4f, and (c) O 1s.

Table S3. The binding energies of the chemical states of the elements present in $CoBi_9O_x$ before and after chronopotentiometric test for 5 hours.

Catalyst	**Binding Energy (eV)**						
	Co $2p_{3/2}$ of Co(II)	Co $2p_{3/2}$ of Co(III)	Bi $4f_{7/2}$ of Bi(III)	Bi $4f_{7/2}$ of Bi(V)	O 1s of O_{lat}	O 1s of O_{vac}	O 1s of O_{OH}
$CoBi_9BiO_x$	779.65	780.79	158.95	159.55	529.86	530.89	-
$CoBi_9BiO_x$ after 5 hours of chronopotentiometric run	779.79	780.96	159.02	160.40	529.95	530.69	531.48

Table S4. Comparison of the electrocatalytic performances of our Bi-doped cobalt oxides for OER in acidic solution with respect to those of notable cobalt oxide-based, acidic OER electrocatalysts reported in the literature.

Catalyst	Overpotential at 10 mA cm^{-2} (mV)	Tafel slope (mV dec^{-1})	Stable hours of catalysis	Electrolyte	Reference
Ce-Co_3O_4	348	84.26	25 h at 10 mA cm^{-2}	0.5 M H_2SO_4	*Inorg. Chem.* **2024**, 63, 4, 1947–1953.
Ir-Co_3O_4	236	52.6	30 h at 10 mA cm^{-2}	0.5 M H_2SO_4	*Nat Commun* **2022**, 13, 7754.
CeO_2-Co_3O_4	423	88.1	50 h at 10 mA cm^{-2}	0.5 M H_2SO_4	*Nat Commun* **2021**, 12, 3036.
Co−Bi−SnO_x/FTO	670	80	216 h at 10 mA cm^{-2}	0.1 M H_2SO_4	*ChemCatChem* **2022**, 14, e202200013.
Co_3O_4/FTO	570	-	12 h at 10 mA cm^{-2}	0.5 M H_2SO_4	*Chem. Mater.* **2017**, 29, 950−957.
Ag-Co_3O_4/FTO	680	219	10 h at 6.5 mA cm^{-2}	0.5 M H_2SO_4	*Renewable Energy* **2018**, 119 54-61.
CeO_2/Co-Ni−P−O_x	262	32.9	5 h at 5 mA cm^{-2}	0.5 M H_2SO_4	*ACS Catal.* **2023**, 13, 5194−5204
$CoSb_2O_6$	760		24 h at 10 mA cm^{-2}	0.5 M H_2SO_4	*ACS Appl. Energy Mater.* **2020**, 3, 5563−5571.
Co_2TiO_4	403	240	10 h	0.5 M H_2SO_4	*Inorg. Chem.* **2019**, 58, 8570−8576.
Co_9BiO_x	**540**	**113**	**45 h at 5 mA cm^{-2}**	**0.1 M $HClO_4$**	**This work**
Co_9BiO_x	**540**	**113**	**25 h at 10 mA cm^{-2}**	**0.1 M $HClO_4$**	**This work**

Synthesis and Results of Bi-Doped Iron Oxides and Bi-Doped Nickel Oxides

To demonstrate the versatility of Bi in enhancing the OER activity of other transition metal oxides, we also synthesized Bi-doped iron oxides and Bi-doped nickel oxides with Fe:Bi or Ni:Bi ratios of 14:1, 9:1, and 2:1 on FTO and then studied their electrocatalytic activity towards acidic OER in the same way, as we did for Bi-doped cobalt oxides. The only difference is in the synthetic protocol used here, which involves nickel(II) nitrate hexahydrate ($Ni(NO_3)_2{\cdot}6H_2O$) or iron(III) nitrate nonahydrate ($Fe(NO_3)_3{\cdot}9H_2O$), respectively, instead of cobalt nitrate hexahydrate ($Co(NO_3)_2{\cdot}6H_2O$).

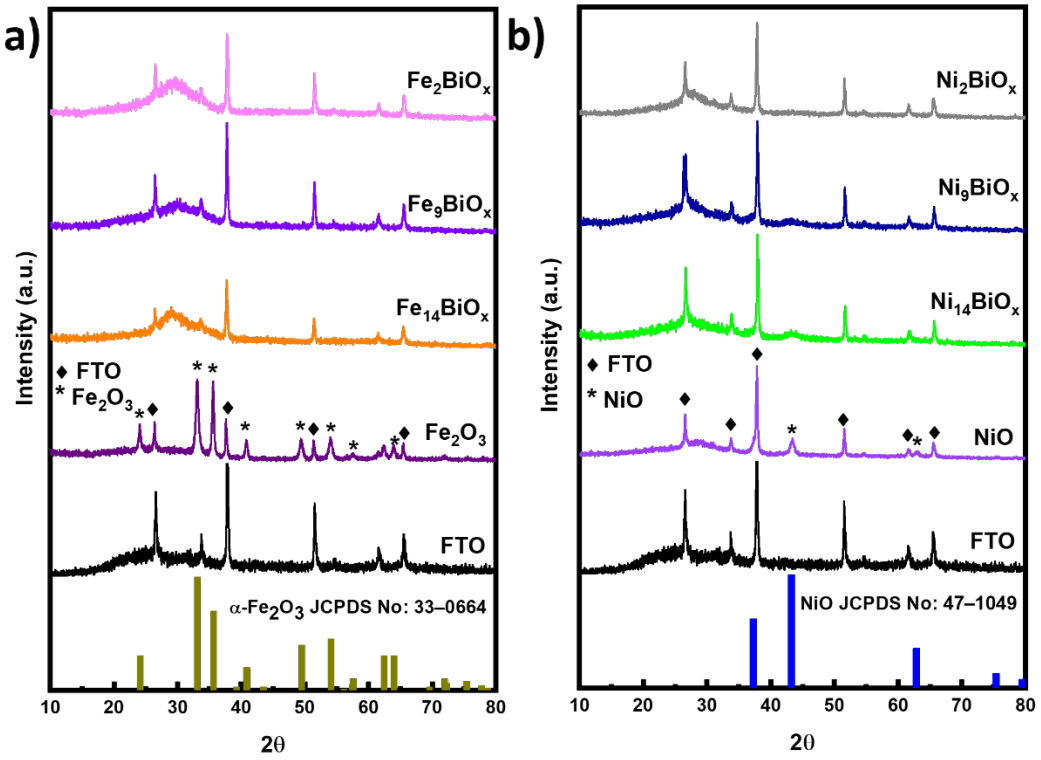

Figure S16. XRD patterns of the Bi-doped iron oxides and Bi-doped nickel oxides catalysts synthesized in situ on FTO and their respective control materials: (a) Fe_2O_3, $Fe_{14}BiO_x$, Fe_9BiO_x, and Fe_2BiO_x and b) NiO, $Ni_{14}BiO_x$, Ni_9BiO_x, and Ni_2BiO_x.

The XRD patterns of these catalysts are displayed in Figure S16. The XRD patterns show that the iron oxide synthesized without Bi dopants is α-Fe_2O_3. Its XRD peaks at 2θ = 24.05, 33.09, 35.58, 40.74, 49.34, 53.97, 57.48, 62.33, and 63.91° correspond to the (012), (104), (110), (113), (024), (116), (018), (214), and (300) crystalline planes of α-Fe_2O_3, respectively (JCPDS No: 33–0664) (Figure S16a).[9,10] However, the XRD patterns of the Bi-doped iron oxides $Fe_{14}BiO_x$, Fe_9BiO_x, and Fe_2BiO_x show peaks corresponding only to FTO, or none corresponding to either α-Fe_2O_3 or Bi_2O_3. So, the synthesis of iron oxide with Bi dopants can produce an amorphous material. Similar results are obtained for pristine nickel oxide and Bi-doped nickel oxides. The XRD pattern of pristine nickel oxide, which does not contain Bi, shows peaks at 2θ = 43.43 and 63.1°, which can be ascribed to (200), and (220) crystal planes of NiO (JCPDS No: 47–1049) (Figure S16b).[11] The XRD patterns of the catalysts

$Ni_{14}BiO_x$, Ni_9BiO_x, and Ni_2BiO_x, which contain Bi, show only a broad peak at 2θ of 43.43° and no new peaks compared with that of NiO. The broad XRD peaks observed in the cases of the Bi-doped nickel oxides is consistent with the formation of an amorphous structures in them. This indicate that the presence of Bi in nickel oxide makes the latter to have amorphous structures, just like what was obtained in the cases of Bi-doped cobalt oxides as well as Bi-doped iron oxides.

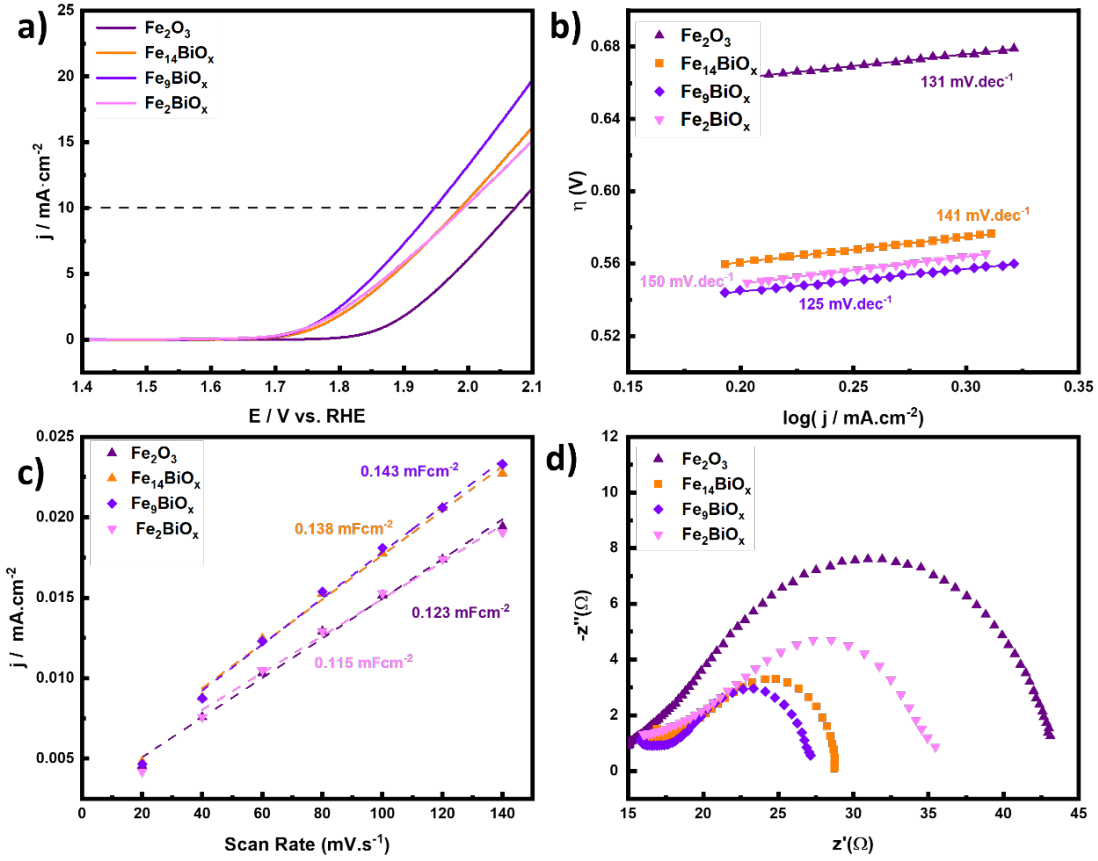

Figure S17. (a) The LSV curves of OER obtained at a scan rate of 5 mV s^{-1} over Fe_2O_3, $Fe_{14}BiO_x$, Fe_9BiO_x, and Fe_2BiO_x electrocatalysts in 0.1 M $HClO_4$ solution. (b) Tafel slopes for the reaction over the catalysts, which are derived from their respective LSV curves. (c) Plots of charging current density obtained from the difference between the anodic and cathodic currents versus scan rates in the non-faradaic region of OER to determine the capacitance of each catalyst. (d) Nyquist plots for Fe_2O_3, $Fe_{14}BiO_x$, Fe_9BiO_x, and Fe_2BiO_x that are obtained from their respective EIS measurements.

The electrocatalytic activities of Bi-doped iron oxides for acidic OER are also investigated using 0.1 M $HClO_4$ as an electrolyte. The LSV curves (Figure S17a) show that iron oxide also exhibits better catalytic activity for OER when it contains Bi. Among them, the catalyst Fe_9BiO_x, which has Fe:Bi ratio of 9:1, requires the lowest overpotential (η = 715 mV) to drive the OER at a current density (j) of 10 mA cm^{-2}. The pristine iron oxide α-Fe_2O_3, in contrast, requires an overpotential of 834 mV to drive the reaction at the same current density. This signifies the ability of Bi in improving the catalytic activity of iron oxide for OER in acidic solution. Comparison of the Tafel plots of all Bi-doped iron oxides and pristine α-Fe_2O_3 shows that Fe_9BiO_x has the lowest

Tafel slope (125 mV dec^{-1}), indicating its most favorable surfaces for OER kinetics in acidic solution (Figure S17b). Similarly, the capacitances measured for the catalysts from their plots of charging current density of the reaction versus scan rate also indicate that Fe_9BiO_x has the highest density of electrochemically accessible active sites (Figure S17c). This means that the catalytic active sites on iron oxide increase when it contains some Bi.

In addition, electrochemical impedance spectroscopy is used to evaluate the overall reaction kinetics of these electrocatalysts. Their Nyquist plots (Figure S17d) show that Fe_9BiO_x has the smallest semicircle among all the catalysts. This indicates that this material has the smallest charge transfer resistance (R_{ct}) and the best overall acidic OER kinetics. These electrochemical studies show that presence of an optimal amount of Bi into iron oxide can greatly enhance the electrocatalytic activity of the latter as well as the OER kinetics over it in acidic media.

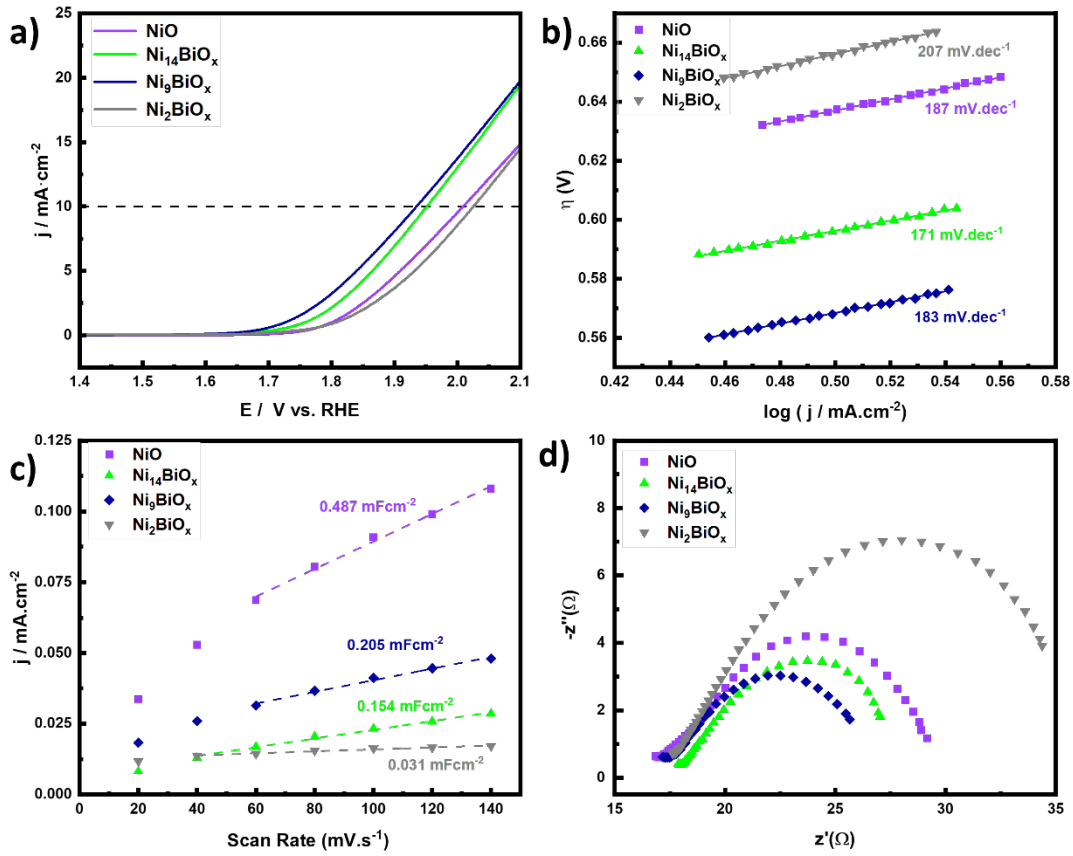

Figure S18. (a) The LSV curves of OER obtained at a scan rate of 5 mV s^{-1} over NiO, $Ni_{14}BiO_x$, Ni_9BiO_x, and Ni_2BiO_x electrocatalysts in 0.1 M $HClO_4$ solution and (b) Tafel slopes of the catalysts derived from their respective LSV curves. (c) Plots of the charging current density of the OER (which is obtained from the difference between the anodic and cathodic currents) versus the scan rate in the non-faradaic region of the reaction to determine the capacitances of the catalysts. (d) Nyquist plots for NiO, $Ni_{14}BiO_x$, Ni_9BiO_x, and Ni_2BiO_x obtained from their respective EIS results.

Similarly, electrochemical studies are carried out for the Bi-doped nickel oxide catalysts. The LSV curves, which is displayed in Figure S18a, show that for Ni_9BiO_x

requires the lowest overpotential (η = 700 mV) to drive the OER at a current density (j) of 10 mA cm^{-2}. The pristine NiO, in contrast, requires an overpotential of 770 mV at 10 mA cm^{-2}. These results indicate that doping Bi into NiO improves the electrocatalytic activity of the latter for OER in acidic media. However, when the Tafel slopes of the Bi-doped nickel oxides and pure NiO are compared with one another, the lowest Tafel slope (171 $mV.dec^{-1}$) is obtained for the catalyst $Ni_{14}BiO_x$, indicating that it enables the fastest kinetic for the OER (Figure S18b). But from the LSV curves, Ni_9BiO_x has lower onset potential for OER than of $Ni_{14}BiO_x$. So, to further understand the properties of these catalysts, we evaluated the density of their active sites by measuring their capacitances. Interestingly, the highest capacitance is obtained for NiO (or all Bi-doped nickel oxides have lower capacitances than NIO) (see Figure S18c). However, low overpotentials and low Tafel slopes are obtained for $Ni_{14}BiO_x$ and Ni_9BiO_x, despite their lower density of active sites.

Additionally, the charge transfer resistances of NiO and Bi-doped nickel oxide catalysts are determined through EIS measurements. The Nyquist plots depicted in Figure S18d indicate that Ni_9BiO_x has the lowest charge transfer resistance. Thus, from the electrochemical studies, it can be said that doping Bi into of nickel oxides improves the electrocatalytic activity of the latter towards acidic OER.

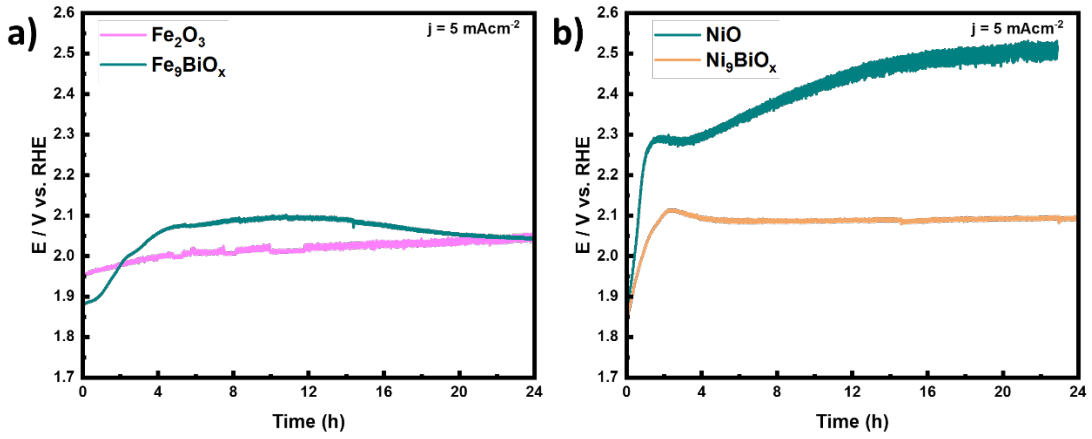

Figure S19. Chronopotentiometric profiles at current density of 5 mA cm^{-2} for OER over a) Fe_2O_3 and Fe_9BiO_x catalysts and b) NiO and Ni_9BiO_x catalysts.

Since the lack of stability of first row transition metal oxides in acidic media is one of the main problems that hinders their application as acidic OER catalysts, we evaluated the stability of the best Bi-doped iron oxide and Bi-doped nickel oxide catalysts as well as their respective pristine oxides (without Bi dopants) using chronopotentiometry. The chronopotentiometric curves of the catalysts at 5 mA cm^{-2} show that both Fe_9BiO_x and Ni_9BiO_x and their respective oxides are not stable even for a few hours during electrocatalysis (Figure S19). Though the presence of Bi in iron oxide and nickel oxide improves their catalytic activities for acidic OER, their lack of stability impedes their practical use as potential OER catalysts. Nevertheless, through the electrochemical studies on Bi-doped cobalt oxides, Bi-doped iron oxides, and Bi-doped nickel oxides, the versatility of Bi dopants in improving the acidic OER activity of first row transition metal oxides have been demonstrated. In the case of Bi-doped

cobalt oxides, we have also shown its stability during acidic OER electrocatalysis. Thus, we believe that our studies will pave the way towards finding a stable low-cost catalyst for acidic OER.

References

1. Kresse, G.; Furthmüller, J. Efficient iterative schemes for ab initio total-energy calculations using a plane-wave basis set. *Phys. Rev. B* **1996,** *54*, 11169-11186.
2. Kresse, G.; Furthmüller, J., Efficiency of ab-initio total energy calculations for metals and semiconductors using a plane-wave basis set. *Comput. Mat. Sci.* **1996,** *6*, 15-50.
3. Kresse, G.; Joubert, D., From ultrasoft pseudopotentials to the projector augmented-wave method. *Phys. Rev. B* **1999,** *59*, 1758-1775.
4. Perdew, J. P.; Burke, K.; Ernzerhof, M., Generalized Gradient Approximation Made Simple. *Phys. Rev. Lett.* **1996,** *77*, 3865-3868.
5. Grimme, S.; Antony, J.; Ehrlich, S.; Krieg, H., A consistent and accurate ab initio parametrization of density functional dispersion correction (DFT-D) for the 94 elements H-Pu. *J. Chem. Phys.* **2010,** *132*, 154104.
6. Zhang, Z.; Tan, G.; Kumar, A.; Liu, H.; Yang, X.; Gao, W.; Bai, L.; Chang, H.; Kuang, Y.; Li, Y.; Sun, X., First-principles study of oxygen evolution on Co_3O_4 with short-range ordered Ir doping. *Mol. Catal.* **2023,** *535*, 112852.
7. Peterson, A. A.; Abild-Pedersen, F.; Studt, F.; Rossmeisl, J.; Nørskov, J. K., How copper catalyzes the electroreduction of carbon dioxide into hydrocarbon fuels. *Energy Environ. Sci.* **2010,** *3* (9), 1311-1315.
8. Wang, V.; Xu, N.; Liu, J.-C.; Tang, G.; Geng, W.-T., VASPKIT: A user-friendly interface facilitating high-throughput computing and analysis using VASP code. *Comput. Phys. Commun.* **2021,** *267*, 108033.
9. Palem, R. R.; Meena, A.; Soni, R.; Meena, J.; Lee, S.-H.; Patil, S. A.; Ansar, S.; Kim, H.-S.; Im, H.; Bathula, C., Fabrication of Fe_2O_3 nanostructure on CNT for oxygen evolution reaction. *Ceram. Int.* **2022,** *48*, 29081-29086.
10. Flak, D.; Chen, Q.; Mun, B. S.; Liu, Z.; Rękas, M.; Braun, A., In situ ambient pressure XPS observation of surface chemistry and electronic structure of α-Fe_2O_3 and γ-Fe$_2$O3 nanoparticles. *Appl. Surf. Sci.* **2018,** *455*, 1019-1028.
11. Goel, R.; Jha, R.; Ravikant, C., Investigating the structural, electrochemical, and optical properties of p-type spherical nickel oxide (NiO) nanoparticles. *J. Phys. Chem. Solids* **2020,** *144*, 109488.